Thermal conductivity depth-profile reconstruction of multilayered cylindrical solids using the thermal-wave Green function method

Guangxi Xie,[1,2] Jie Zhang,[1] Liwang Liu,[1] Chinhua Wang,[1,a)] and Andreas Mandelis[3]
[1]*Key Lab of Modern Optical Technologies of Jiangsu Province, Institute of Modern Optical Technologies, Soochow University, Suzhou, Jiangsu, 215006*
[2]*Department of Physics, Jiangnan University, Wuxi, Jiangsu, 214122, People's Republic of China*
[3]*Center for Advanced Diffusion-Wave Technologies (CADIFT), Department of Mechanical and Industrial Engineering, University of Toronto M5S 3G8, Ontario, Canada*

(Received 13 February 2011; accepted 28 April 2011; published online 13 June 2011)

In this paper, a theoretical model for characterizing solid multi-layered cylindrical samples illuminated by a modulated uniform incident beam is developed by means of the Green function method. The specific Green function for the multi-layered cylindrical structure is derived and an analytical expression for the thermal-wave field in such a cylindrical sample is presented. The thermal-wave field of an inhomogeneous cylindrical sample irradiated with incident light of arbitrary angular and/or radial intensity distribution was obtained using this theoretical model. Furthermore, experimental validation is also presented in the form of experimental results with steel cylinders of various diameters. © *2011 American Institute of Physics*. [doi:10.1063/1.3595674]

I. INTRODUCTION

Since their emergence in the early 1980s, photothermal techniques have become very powerful tools for the thermophysical characterization and nondestructive evaluation (NDE) of a wide variety of materials.[1–4] These techniques are based on the generation and detection of thermal waves excited by an incident energy source in the sample. Various photothermal measurement schemes, such as infrared radiometry, photothermal beam displacement (mirage effect), photopyroelectric detection, photothermal reflectance, etc., have been developed to detect thermal waves and therefore, extract material thermophysical properties and internal structure information. However, for decades, research in photothermal techniques has been restricted to samples with flat surfaces. Recently, significant and rapid progress has been made on studies of samples with curved surfaces.[5–11] Wang *et al*. investigated both theoretically and experimentally homogenous and bilayered cylindrical and spherical samples[5–8] by the Green function method which is a well-known formalism for solving various boundary-value problems, including the thermal-wave fields of diverse geometries. The thermal-wave field of a sample with incident light of arbitrary angular and/or radial intensity distribution can be obtained once the Green function is determined for a specific geometry. Subsequently, Salazar *et al*. developed a technique for characterizing the thermal-wave fields of multilayer cylindrical and spherical samples using the quadrupole method,[9–11] in which a linear relation between temperature and incident heat flux at the outer and inner surfaces of the sample is used to derive the thermal-wave fields of layered structures. The quadrupole method, however, is limited to samples with cylindrical or spherical symmetry and can only calculate the temperature on the sample surface, which sometimes limits the general applicability of the theoretical model. In most previous work in the photothermal field, the depth-profile reconstructions of the thermophysical parameters were usually implemented using inverse-problem methods.[12–15] In those studies, the samples were limited to the flat surface and the measurement scheme was limited to one-dimension (1D) in which the incident laser beam was expanded to be large enough when compared to the thermal diffusion length, so as to simplify the mathematical formulism and computational algorithm. With the increasing application of photothermal techniques to nonflat samples, inverse-problem method may encounter difficulties due to the complicated 3D modeling and the computational algorithm related to the geometry and the beam profile. In this paper, we develop a theoretical model for characterizing solid multi-layered cylindrical samples using the Green function method. We first develop the thermal-wave Green function for the multi-layered structure geometry, and then we present an analytical expression for the thermal-wave field in such a cylindrical solid. The earlier theoretical models[5,8,9] for the two-layer or homogeneous cylinder can be used to demonstrate the validity of this multilayered model in the limit of two-layers. Finally, experimental validation is presented in which a group of cylinders of various diameters are measured and fitted to the theoretical model. In contrast to the inverse-problem method, a "forward" data-fitting process[16] is employed to reconstruct the depth profile of the thermophysical parameter. The experimental results show good agreement with the theoretical model. It is expected that this theoretical model, which is capable of providing general temperature field at any location of the sample, will be useful in quantitative thermophysical characterization of multi-layered cylindrical samples.

a)Electronic mail: chinhua.wang@suda.edu.cn.

II. THEORY

The thermal-wave field of a multi-layered cylindrical solid sample with outer radius r_N and inner radius r_{N-1}, $r_{N-2}, \ldots, r_1$, $(b = r_N > r_{N-1} > r_{N-2} > \cdots > r_1 = a)$ can be derived by the Green function method. The geometry and coordinates of the boundary-value problem are shown in Fig. 1. The thermal conductivity and diffusivity of regions I and II, III,…, N are denoted by (k_1, α_1) and (k_2, α_2),…, (k_N, α_N), respectively. The exciting laser beam, which is taken to be of uniform intensity for simplicity and subtends angle θ_0, Figure 1, impinges on the cylindrical surface. The harmonic thermal-wave equation for the material under investigation in region N can be written as:

$$\nabla^2 T(\vec{r},\omega) - \sigma_N^2(\omega)\cdot T(\vec{r},\omega) = -\frac{1}{k_N} Q(\vec{r},\omega) \tag{1}$$

where, $\sigma_N(\omega) = (i\omega/\alpha_N)^{1/2} = (1+i)\cdot\sqrt{\omega/2\alpha_N}$ is the complex thermal wave-number of region N, ω is the angular modulation frequency of the laser beam and $Q(\vec{r},\omega)$ is the volume thermal source at coordinates $\vec{r} = (r,\varphi)$ inside the material. Based on the Green function method, the general solution for Eq. (1) can be expressed as:[17]

$$\begin{aligned} T(\vec{r},\omega) = {} & \left(\frac{\alpha_N}{k_N}\right)\iiint_{V_0} Q(\vec{r}_0,\omega)\cdot G^{(N)}(\vec{r}|\vec{r}_0,\omega)\cdot dV_0 \\ & + \alpha_N \oint_{S_0} [G^{(N)}(\vec{r}|\vec{r}_0^{\,s},\omega)\cdot \vec{\nabla}_0 T(\vec{r}_0^{\,s},\omega) \\ & \cdot \vec{\nabla}_0 G^{(N)}(\vec{r}|\vec{r}_0^{\,s},\omega)]\cdot d\vec{S}_0, \end{aligned} \tag{2}$$

where S_0 is the surface surrounding the domain volume V_0 (i.e., region N), which includes the harmonic source $Q(\vec{r}_0,\omega)$; $\vec{r}_s$, $\vec{r}_0^{\,s}$ is the source coordinate point in the bulk and on the surface S_0, respectively. Here $d\vec{S}_0 = \vec{n}\cdot dS_0$ with $\vec{n}$ being the outward unit vector normal to the boundary surface S_0, as shown in Fig. 1. $G^{(N)}$ is the thermal-wave Green function with units of $[s/m^3]$. Equation (2) gives the most general formula to evaluate the thermal-wave field in the investigated region under investigation under arbitrary boundary conditions. It is noted that, in most cases, Eq. (2) can be simplified depending on specific material properties and boundary conditions imposed on the solid. For solids with high optical absorption coefficients, such as metallic samples, the volume source can be neglected $[Q(\vec{r}_0,\omega)\equiv 0]$. In this paper, we focus on metallic (opaque) materials. Moreover, considering that illumination of the outer surface by a laser beam leads to optical-to-thermal energy conversion essentially at the surface, and that the thermal coupling coefficient between a metallic solid and the surrounding gas (air) is on the order of 10^{-3} (Ref. 18), the adiabatic second-kind (Neumann) boundary condition at the outer surface can be applied. Furthermore, to convert the improper Green function to a proper one which can be applied to multi-layered solids with nonhomogeneous interface conditions,[17] we assume a third-kind boundary condition on the inner surface of region N at $r = r_{N-1}$, as discussed below. The homogeneous boundary conditions for the appropriate Green function and inhomogeneous boundary conditions for the thermal-wave field, respectively, can be written as:

$$k_N\vec{n}\bullet\nabla G^{(N)}(\vec{r}|\vec{r}_0,\omega)|_{r=r_{N-1}} = h_{N-1}G^{(N)}(\vec{r}|\vec{r}_0,\omega)|_{r=r_{N-1}} \tag{3a}$$

$$k_N\vec{n}\bullet\nabla G^{(N)}(\vec{r}|\vec{r}_0,\omega)|_{r=r_N} = 0 \tag{3b}$$

$$\begin{aligned} -k_N\vec{n}\bullet\nabla T(\vec{r}|\vec{r}_0,\omega)|_{r=r_{N-1}} = {} & F_{N-1}(\vec{r}|\vec{r}_0,\omega) \\ & - h_{N-1}T(\vec{r}|\vec{r}_0,\omega)|_{r=r_{N-1}} \end{aligned} \tag{4a}$$

$$k_N\vec{n}\bullet\nabla T(\vec{r}|\vec{r}_0,\omega)|_{r=r_N} = F_N(\vec{r}|\vec{r}_0,\omega)|_{r=r_N}. \tag{4b}$$

Here, h_{N-1} $[Wm^{-2}K^{-1}]$ is the heat transfer coefficient at the inner surface S_{N-1}; F_{N-1} and F_N are the heat fluxes $[Wm^{-2}]$ imposed on the inner and outer surface, respectively. Therefore, in the absence of volume thermal sources in region N and in the underlying region $N-1$, and with the homogeneous boundary conditions for the Green function shown in Eqs. (3) and (4), the general thermal-wave field represented by Eq. (2) reduces to:

$$\begin{aligned} T(\vec{r},\varphi,\omega) = {} & -\frac{\alpha_N}{k_N}\oint_{S_{N-1}} F_{N-1}(\vec{r}_0^{\,s},\omega)\cdot G^{(N)}(\vec{r}|\vec{r}_0^{\,s},\omega)\cdot d\vec{S}_0 \\ & + \frac{\alpha_N}{k_N}\oint_{S_N} F_N(\vec{r}_0^{\,s},\omega)\cdot G^{(N)}(\vec{r}|\vec{r}_0^{\,s},\omega)\cdot d\vec{S}_0, \end{aligned} \tag{5}$$

where, $G^{(N)}(\vec{r}\,|\vec{r}_0,\omega)$ is the Green function for region N which must be derived so as to satisfy the appropriate boundary conditions. It should be emphasized that the condition for Eq. (2) to be reduced to Eq. (5) is that the Green function must be proper (i.e., homogeneous boundary conditions must be satisfied at all surfaces enclosing the volume V_0).

The details of the derivation of the Green function for the specified geometry are given in the Appendix. Section 1 of the Appendix develops the Green function in region N, and the spatial impulse-response function, i.e., the improper Green function in regions $N-$I,…, II and I, respectively, for a multi-layer concentric cylindrical structure. The relevant Green function to be used in the exterior region $r_{N-1}\le r\le r_N$ is Eq. (A32). However, great care must be taken since the Green-function derivation for region N has employed a nonhomogeneous (continuity) boundary condition at $r = r_{N-1}$. Therefore, the function Eq. (A32) is an

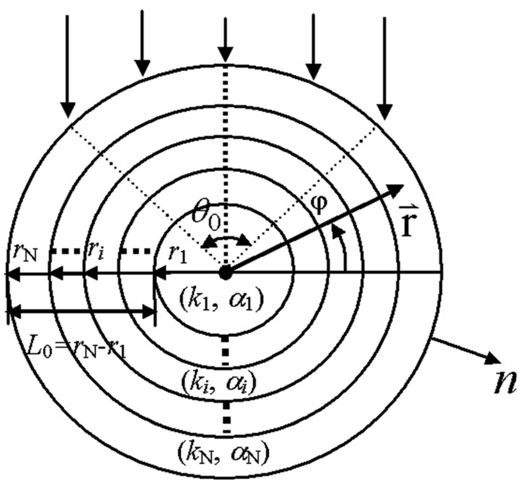

FIG. 1. The geometry and coordinates of the multi-layered cylindrical samples.

improper Green's function.[17] As a result, it cannot be applied readily to obtain the thermal-wave field in region N, because it does not satisfy the requisite homogeneous boundary condition at $r = r_{N-1}$ to validate the field Eq. (5). A proper Green function for the equivalent exterior region N, which satisfies a homogeneous third-kind boundary condition at $r = r_{N-1}$, must be used instead. This Green function is given by Eq. (A43). However, in Eq. (A43), there is no direct thermal-wave coupling to the underlayer in region (N-I). There is only an indirect involvement of the inner region at thermal equilibrium through the heat transfer coefficient h_{N-1}. A direct involvement of region (N-I) into the proper Green function for region N, Eq. (A43), can be introduced through correlating the thermal parameters (k_1, α_1) in Eq. (A32) in region N to the (otherwise arbitrary) constant h_{N-1} in Eq. (A43). This line of reasoning leads to the equivalence relations (A49) and (A50) in Sec. 2 of the Appendix. Those relations show that for the specified value of h_{N-1}, the proper Green function Eq. (A43), and its integral, Eq. (5), can be used as an equivalent Green function and as a valid thermal-wave field distribution integral, respectively, to describe the effects of the multi-layer, despite the nonhomogeneous interior boundary conditions. In summary, the appropriate Green function to be used in Eq. (5) can finally be written with the observation coordinate, r, as the running variable in the form:

$$G^{(N)}(\vec{r}|\vec{r}_0;\omega) = \frac{1}{2\pi\alpha_N}\sum_{m=-\infty}^{\infty}\frac{e^{im(\varphi-\varphi_0)}}{[Y_m(r_N) - X_m(r_{N-1})]} \times \begin{cases} [K_m(\sigma_N r_0) - Y_m(r_N)\cdot I_m(\sigma_N r_0)][K_m(\sigma_N r) - X_m(r_{N-1})\cdot I_m(\sigma_N r)], (r_{N-1} \le r \le r_0) \\ [K_m(\sigma_N r_0) - X_m(r_{N-1})\cdot I_m(\sigma_N r_0)][K_m(\sigma_N r) - Y_m(r_N)\cdot I_m(\sigma_N r)], (r_0 \le r \le r_N) \end{cases} \tag{6}$$

where

$$X_m(r_{N-1}) \equiv \frac{[K'_m(\sigma_N r_{N-1}) - \lambda_{N-1}\cdot K_m(\sigma_N r_{N-1})]}{[I'_m(\sigma_N r_{N-1}) - \lambda_{N-1}\cdot I_m(\sigma_N r_{N-1})]}, \tag{7}$$

$$Y_m(r_N) \equiv \frac{K'_m(\sigma_N r_N) + m_N\cdot K_m(\sigma_N r_N)}{I'_m(\sigma_N r_N) + m_N\cdot I_m(\sigma_N r_N)} \to \frac{K'_m(\sigma_N r_N)}{I'_m(\sigma_N r_N)}, \quad (m_N = 0) \tag{8}$$

$$\lambda_{N-1} \equiv \frac{[I'_m(\sigma_{N-1}r_{N-1}) + K'_m(\sigma_{N-1}r_{n-1})\cdot\gamma_{(N-1)\cdots 321}]}{\beta_{N,(N-1)}[I_m(\sigma_{N-1}r_{N-1}) + K_m(\sigma_{N-1}r_{N-1})\cdot\gamma_{(N-1)\cdots 321}]},$$

and $\quad \beta_{N,(N-1)} \equiv k_N/k_{N-1}. \quad (9)$

Here, $m = 0, 1, 2, \ldots;$ and $\sigma_j = (1+i)\sqrt{\omega/2\alpha_j}, (j = 1, 2, \ldots, N)$ are thermal wave numbers; $\gamma_{N,(N-1)\cdots 321} \equiv \left[t_{21}^{(N)}/t_{11}^{(N)}\right]$ (given in the Appendix); $I_m(z)$, $K_m(z)$ are the complex-argument modified Bessel functions of the first and the second kind of order m, respectively.

In view of the structure of Eq. (5), the prescribed thermal-wave fluxes F_{N-1} and F_N at the inner and outer surface, respectively, must be specified. In our case, there is no incident flux prescribed at the inner surface $r = r_{N-1}$, therefore

$$F_{N-1}(\vec{r}_0^s, \omega) = 0. \tag{10}$$

Assuming that the incident light intensity on the exterior surface is uniform, in conformity with standard collimated experimental photothermal configurations such as laser infrared photothermal radiometry (PTR), the thermal-wave flux on that surface must be weighted using a projection factor in the form of the cosine of the incident uniform light intensity which can be expressed as:

$$F_N(\vec{r}_N^s, \omega) = \begin{cases} F_0\cos\left(\frac{\pi}{2} - \varphi_0\right), -\theta_0/2 \le \varphi_0 \le \theta_0/2 \\ 0, \text{otherwise} \end{cases}. \tag{11}$$

It should be noted that the expression of Eq. (11) may be changed depending on the incident beam profile. This theoretical method is valid for any arbitrary incident beam profile by changing the expression of Eq. (11).

Substituting Eqs. (10) and (11) into Eq. (5), we obtain:

$$T(\vec{r}, \varphi, \omega) = \frac{\alpha_N.F_0}{k_N}\oint_{S_N} G^{(N)}(\vec{r}|\vec{r}_0^s, \omega)\cdot\cos\left(\frac{\pi}{2} - \varphi_0\right)\cdot dS_0\,. \tag{12}$$

Where, $dS_0 = r_N d\varphi_0$. Now interchanging $(r, \varphi) \leftrightarrow (r_0, \varphi_0)$ in the Green function, Eq. (6), so as to allow integrations over the source coordinates (r_0, φ_0) and letting $r_0 = r_N$ (surface source), Eq. (12) becomes

$$T(r, \varphi, \omega) = \frac{F_0}{2\pi k_N}\int_{-\theta_0/2+\pi/2}^{\theta_0/2+\pi/2} \times \sum_{m=-\infty}^{+\infty}\frac{[K_m(\sigma_N r) - X_m(r_{N-1})I_m(\sigma_N r)]}{I'_m(\sigma_N r_N)[Y_m(r_N) - X_m(r_{N-1})]} \times e^{im(\varphi_0-\varphi)}\cos(\pi/2 - \varphi_0)d\varphi_0. \tag{13}$$

Using the identity

$$\sum_{m=-\infty}^{+\infty} e^{im(\phi_0-\phi)} = 1 + 2\sum_{m=1}^{\infty}\cos[m(\varphi - \varphi_0)]$$

and $\quad I_{-\nu}(z) = I_\nu(z);\ K_{-\nu}(z) = K_\nu(z) \quad (14)$

after some algebraic manipulation, one finally obtains the thermal-wave field in region N:

$$T(r,\varphi,\omega)=\frac{F_0}{2\pi k_N}\left\{2\frac{[K_0(\sigma_N r)-X_0(r_{N-1})I_0(\sigma_N r)]}{I_0'(\sigma_N r_N)[Y_0(r_N)-X_0(r_{N-1})]}\cdot\sin\frac{\theta_0}{2}\right.$$
$$+\frac{[K_1(\sigma_N r)-X_1(r_{N-1})I_1(\sigma_N r)]}{I_1'(\sigma_N r_N)[Y_1(r_N)-X_1(r_{N-1})]}.(\theta_0+\sin\theta_0)$$
$$\times\cos\left(\frac{\pi}{2}-\varphi\right)$$
$$+2\sum_{m=2}^{\infty}\frac{[K_m(\sigma_N r)-X_m(r_{N-1})I_m(\sigma_N r)]}{I_m'(\sigma_N r_N)[Y_m(r_N)-X_m(r_{N-1})]}$$
$$\times\cos\left[\frac{m}{2}(\pi-2\varphi)\right]\cdot\left[\frac{\sin[(m+1)\theta_0/2]}{m+1}\right.$$
$$\left.\left.+\frac{\sin[(m-1)\theta_0/2]}{m-1}\right]\right\}. \tag{15}$$

From the structure of this expression, it is seen that the frequency dependence of the thermal-wave field of a multi-layered cylinder under illumination with a uniform light beam is a strong function of the material thermal diffusivity as well as geometrical factors of the solid.

If the exciting beam is a Gaussian laser beam, the thermal-wave flux on that surface can be expressed as:

$$F_N(\vec{r}_N^s,\omega)=\begin{cases}F_0\cos(\pi/2-\varphi_0)e^{-\left(\frac{b\cos\varphi_0}{w}\right)^2}, & -\theta_0/2\le\varphi_0\le\theta_0/2\\ 0, & \text{otherwise}\end{cases}. \tag{16}$$

Here b is the radius of cylindrical rod, and w is the spotsize of the laser beam

Then the harmonic thermal-wave equation for the material under investigation in region N can be written as:

$$T(r,\varphi,\omega)=\frac{F_0}{2\pi k_N}\int_{-\theta_0/2+\pi/2}^{\theta_0/2+\pi/2}\sum_{m=-\infty}^{+\infty}$$
$$\times\frac{[K_m(\sigma_N r)-X_m(r_{N-1})I_m(\sigma_N r)]}{I_m'(\sigma_N r_N)[Y_m(r_N)-X_m(r_{N-1})]}$$
$$\times e^{im(\varphi_0-\varphi)}\cos(\pi/2-\varphi_0)e^{-\left(\frac{b\cos\varphi_0}{\omega}\right)^2}d\varphi_0. \tag{17}$$

Using Eq. (14), the thermal-wave field in region N can be obtained:

$$T(r,\varphi,\omega)=\frac{F_0}{2\pi k_N}\left\{\frac{[K_0(\sigma_N r)-X_0(r_{N-1})I_0(\sigma_N r)]}{I_0'(\sigma_N r_N)[Y_0(r_N)-X_0(r_{N-1})]}\cdot\right.$$
$$\times\int_{-\theta_0/2+\pi/2}^{\theta_0/2+\pi/2}\sin\varphi_0 e^{-\left(\frac{b\cos\varphi_0}{w}\right)^2}d\varphi_0$$
$$+2\sum_{m=1}^{\infty}\frac{[K_m(\sigma_N r)-X_m(r_{N-1})I_m(\sigma_N r)]}{I_m'(\sigma_N r_N)[Y_m(r_N)-X_m(r_{N-1})]}$$
$$\left.\times\int_{-\theta_0/2+\pi/2}^{\theta_0/2+\pi/2}\cos[m(\varphi_0-\varphi)]\sin\varphi_0 e^{-\left(\frac{b\cos\varphi_0}{w}\right)^2}d\varphi_0\right\}. \tag{18}$$

Based on Eq. (18), the thermal-wave fields of a cylindrical solid with the Gaussian beam illumination can be obtained readily with a numerical integration.

III. NUMERICAL SIMULATIONS

A. Special cases

In Sec. II, we developed the thermal-wave Green function for a multi-layered cylinder and gave the analytical expression, Eq. (15), for the thermal-wave field in such a cylindrical solid. In this Section, we will focus on verification of this theoretical model though special-case simplification and comparison. Prior to this, it is noted that although Eq. (15) gives the thermal-wave field at any point inside the cylinder, using the PTR technique with an opaque solid only the thermal-wave field from the sample surface can be detected.[19] Therefore, our investigations and simulations will be restricted to the sample surface at $r = r_N$. In all simulations, the amplitude and phase of the surface thermal-wave field are normalized to the corresponding amplitude and phase of a one-layer cylinder sample of the same material (AISI 1018 steel). The thermophysical parameters of AISI 1018 steel are $k = 51.9W/mK$, $\alpha = 13.57\times10^{-6}m^2/s$ (Ref. 20).

First, a couple of analytical checks of limiting cases in Eq. (15) are in order. It is obvious that if $\theta_0 = 0$, i.e., no light is incident on the surface, the thermal-wave field $T(\vec{r},\varphi,\omega)=0$, as expected. Next, as another check, Eq. (15) can be easily reduced to a single-layer model, i.e., a homogeneous cylinder, if we set parameters (k_1,α_1), (k_2,α_2),…, (k_{N-1},α_{N-1}) in regions I, II,…,(N-I) equal to parameters (k_N,α_N) in region N, i.e., $(k_1,\alpha_1)=(k_2,\alpha_2)=\cdots=(k_N,\alpha_N)$. The frequency dependence of the surface thermal-wave field of a solid uniform cylinder [the North Pole point, $\varphi=(\pi/2)$] is simulated in this manner and is shown in Fig. 2. In the simulations, two cylindrical solids with the same diameter (10 mm), but made of different materials (aluminum and copper) are investigated in the limit where the incident light beam is large enough to cover the whole projectional surface of the cylindrical solid, i.e., $\theta_0=\pi$. The other parameters used in the simulations are k= 401 W/mK, $\alpha=112.34\times10^{-6}\,m^2/s$ for copper and $k = 204$ W/mK, $\alpha=84.18\times10^{-6}$ m^2/s for aluminum. In addition, the same simulations performed with the theoretical model developed in Ref. 5 are also present for comparison (solid lines). It can be seen that both the amplitude and phase channel of each sample calculated with the model of Eq. (15) in the limit of a single layer and those using the actual single layer expression show perfect agreement. The model developed in Ref. 5 has been found to be suitable for interpreting PTR measurements. In summary, the multi-layer cylinder photothermal theoretical model of Eq. (15) exhibits the correct expected behavior in the limit of a single-layer cylinder.

Equation (15) can also be reduced to a two-layer model by assuming parameters (k_1,α_1), (k_2,α_2),…, (k_{N-2},α_{N-2}) in region I, II,…,(N-II) are equal to parameters (k_{N-1},α_{N-1}) in region N-I, i.e., $(k_1,\alpha_1)=(k_2,\alpha_2)=\cdots=(k_{N-1},\alpha_{N-1})$. Under the same illumination and measurement geometry,

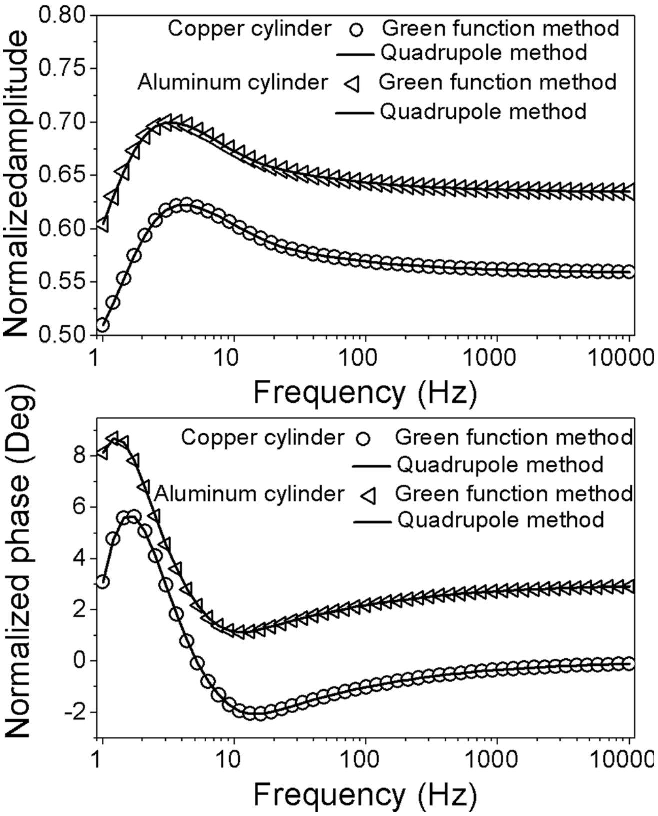

FIG. 2. The frequency dependence of thermal-wave field from solid cylinders simulated by this single layer model from degeneration. Sample A is the cylinder rod coated with copper, and sample B is the cylinder rod coated with aluminum.

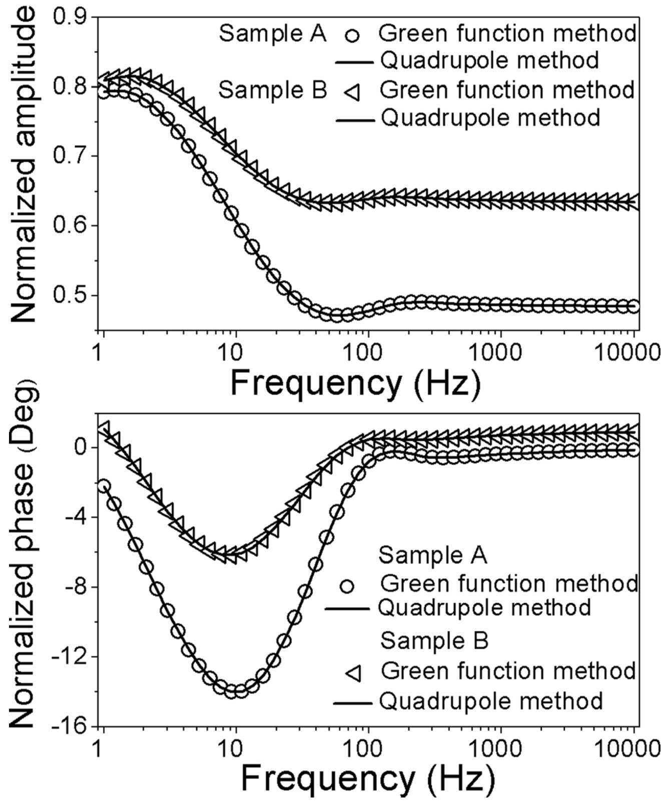

FIG. 3. The frequency dependence of surface thermal-wave field from two-layered solids cylinders. Sample A is a steel rod coated with copper and sample B is a steel rod coated with aluminum.

two AISI 1018 steel rods coated with aluminum and copper respectively are considered, with the common diameter of the two solids equal to 10 mm and coating thickness 1 mm. The surface thermal-wave fields in the two-layer solid cylinders illuminated by modulated light were calculated and Fig. 3 shows the frequency dependence. The symbols are results based on the present model, Eq. (15) in the limit of two layers and the solid lines were calculated using the two-layer model developed in Ref. 9 for comparison. The results are identical throughout the entire frequency range. The foregoing special cases are proof that the generalized complicated model of multi-layered cylinders yields the expected results in a number of important limiting cases. Indeed, the agreement involves both our own earlier results[6] and those obtained with the model developed using the quadrupole method.[9]

B. General case

Simulations involving the full multi-layered model are now presented. Using the same illumination and measurement geometry as above, two AISI 1018 steel rods with various case hardened depths are investigated. They have a 10-mm diameter and different thermal conductivity depth profiles. We assume that the radial thermal conductivity of the inhomogeneous layer in the multilayered rods varies continuously with the depth dependence:[18]

$$k(r) = k_0\left(\frac{1+\Delta e^{-Qr}}{1+\Delta}\right)^2, \text{ with } \Delta = \frac{1-\sqrt{k'/k_0}}{\sqrt{k'/k_0}-e^{-QL_0}}, \quad (19)$$

where k_0 and k' represent the thermal conductivity of the outermost layer and innermost layer, respectively, L_0 is the total thickness of the inhomogeneous surface layer (i.e., $r_N - r_1$,) and exponent Q represents the thermal gradient. The assumed depth profile ansatz Eq. (19) is capable of expressing arbitrary monotonic depth profiles if parameters are properly chosen and has been extensively employed in thermal-wave inverse problem reconstruction techniques. Figure 4 shows the assumed thermal conductivity depth

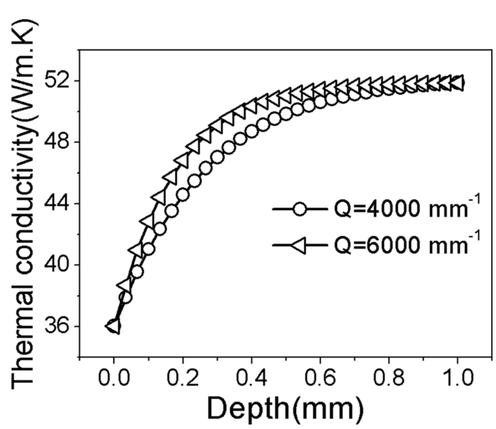

FIG. 4. The assumed thermal conductivity depth profiles of two solid cylindrical rods with different thermal gradients, Q [mm^{-1}].

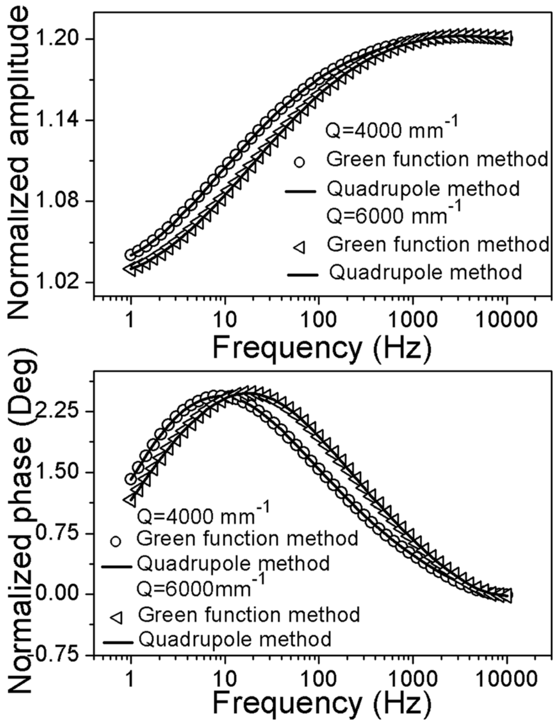

FIG. 5. Comparison of the frequency dependence of surface thermal-wave field calculated by the Green function theoretical model and by the quadrupole method.

profiles of the two rods. The thermal conductivity of the inhomogeneous layer is continuously increased from $k = 36.05\,W/mK$ (at the surface) to the saturated value $k' = 51.9\,W/mK$ at $L_0 (L_0 = 1mm)$ inside the material but with different gradients for the two rods; $Q = 4000(1/mm)$ and $6000(1/mm)$, respectively. Figure 5 is the comparison of the frequency dependence of the surface thermal-wave field in a cylinder made of AISI 1018 steel calculated by the Green function theoretical model, Eq. (15) (symbols) and the quadrupole method (solid line) in Ref. 10. In Fig. 5, cylinders with the continuously variable thermal conductivity depth profiles of Fig. 4 are considered, however, the use of the discrete multiple layer formula Eq. (19) necessitated the approximation of the continuous profile with a step profile. For each virtual slice, j, $1 \le j \le N$ (usually for $L_0 = 1$ mm, $N = 30$ is sufficient to describe a continuous profile) the value of $k(r) = k(r_j)$ is calculated by using Eq. (19) in a stepwise manner for each slice with radial limits $r_j \le r \le r_{j+1}$. The frequency scans of Fig. 5 are normalized by those of a corresponding single-layer cylinder of the same material with the same outer radius and conductivity equal to 51.9 W/mK. It is further seen in Fig. 5 that both amplitude and phase curves calculated with the Green function model completely overlap those curves based on the quadrupole method over the entire frequency range. This indicates that both theoretical models are suitable for characterizing multi-layered cylindrical samples using the PTR technique. However, the advantage of the Green function method is the capability of providing more general temperature field at any points of the sample and also the possible extension of the current simple cylindrical or spherical samples to other geometrical samples.

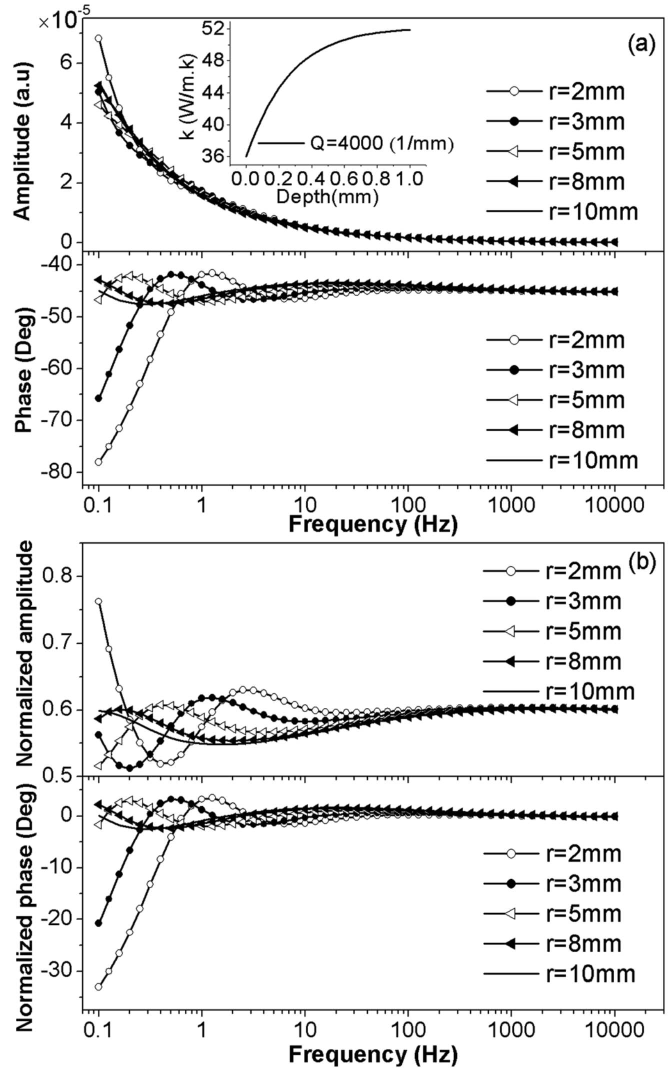

FIG. 6. Effect of cylindrical radius on the photothermal signal with a uniform illumination profile. The inset shows the depth profile of the thermal conductivity. (a) unnormalized amplitude and phase; and (b) normalized amplitude and phase.

Figure 6(a) shows the effect of the cylindrical radius on the photothermal signal with a uniform incident beam profile. All the samples are assumed to have the same inhomogeneous layer as if they were experiencing the same hardening process. The parameters of the thermal conductivity profile of the inhomogeneous layer are: $Q = 4000(1/mm)$, $L_0 = 1mm$, $k_0 = 51.9\,W/mK$, and $k_N = 36.05\,W/mK$. It is seen that both amplitude and phase are sensitive to the radius of the cylindrical sample. Figure 6(b) shows the effect of cylindrical radius on the normalized signal. The amplitude and the phase of the surface-temperature oscillation of the cylindrical samples are normalized to the corresponding amplitude and phase of a flat surface of a semi-infinitely thick sample of the same material as the core part of the cylinder sample in order to see the effects of the curved surface with an optimal contrast. The amplitude and the phase of a flat surface are calculated based on the well-known 1D theoretical model,[17] which exhibits the well-known dependence of the amplitude on the inverse of the square root of the frequency and a constant $\pi/4$ phase lag of the temperature

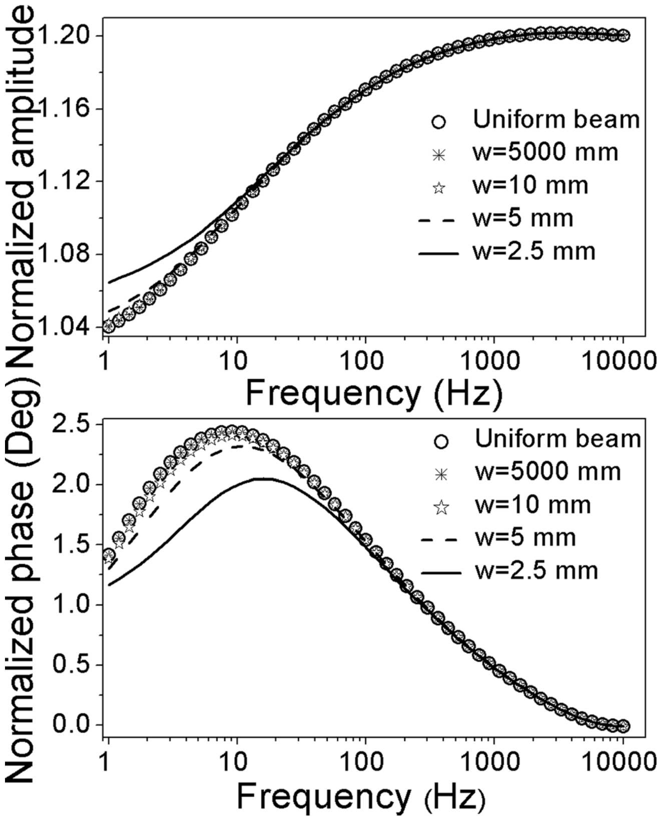

FIG. 7. The frequency dependence of the surface thermal-wave field from multi-layered solid cylinders illuminated by Gaussian beams of various spotsizes. The curves are normalized with a single-layer cylindrical rod of the same material and conductivity equal to 51.9 W/mK.

oscillation with respect to the incident thermal flux. As expected, both normalized amplitude and phase of various diameters are toward to that of the flat surface at high frequencies because of the very short thermal diffusion length at high frequencies when compared with the cylindrical radius of curvature.

Finally, we present the thermal-wave field of a surface illuminated by a Gaussian laser beam. In the simulation, the radii of the rods are assumed to be 10 mm, and the spotsize w is assumed to be 2.5 mm, 5 mm, 10 mm and 5000 mm (i.e., close to infinite), respectively. The parameters of the profile of the thermal conductivity of the inhomogeneous layer are: $Q = 4000(1/mm)$, and $L_0 = 1\,mm$. The simulation results are shown in Fig. 7. It is seen that as the spotsize increases, both amplitude and phase move toward the response of cylinders illuminated with a homogeneous beam. When the laser spotsize $w = 5000\,mm$, the two lines overlap, as expected, because the beam spatial profile distribution converges to uniform. The Green-function sensitivity to beam spotsize demonstrates the capability of this mathematical approach to deal with arbitrary incident beam profiles.

IV. EXPERIMENTAL AND RESULTS

The experimental PTR setup is shown in Fig. 8. The optical excitation source was a high-power semiconductor laser, the emitted power of which was modulated by a periodic current driver. The harmonic infrared radiation from the

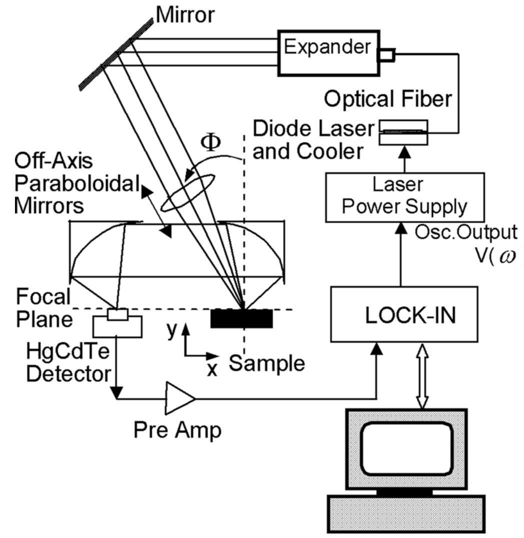

FIG. 8. The experimental PTR setup.

sample surface was collected by an off-axis paraboloidal mirror system and detected by a HgCdTe detector (EG&G Judson). The signal from the detector was preamplified and then fed into a lock-in amplifier (EG&G Instruments) interfaced with a personal computer. Two sets of cylindrical AISI1020 steel samples (composition: 0.18%–0.23%C, 0.3%–0.6%Mn) were machined with radii ranging from 2 to 16 mm. One set of samples went through a case hardening (carburizing) process as one batch to ensure the same case depth profile, with a nominal case depth of 0.04 in. Carburization is a heat treating process in which iron or steel is heated in the presence of another material (in the range of 900–950°C) which liberates carbon as it decomposes. Depending on the amount of time and temperature, the affected area can vary in carbon content. Longer carburizing times and higher temperatures lead to greater carbon diffusion into the part as well as increased depth of carbon diffusion. When the iron or steel is cooled rapidly by quenching,

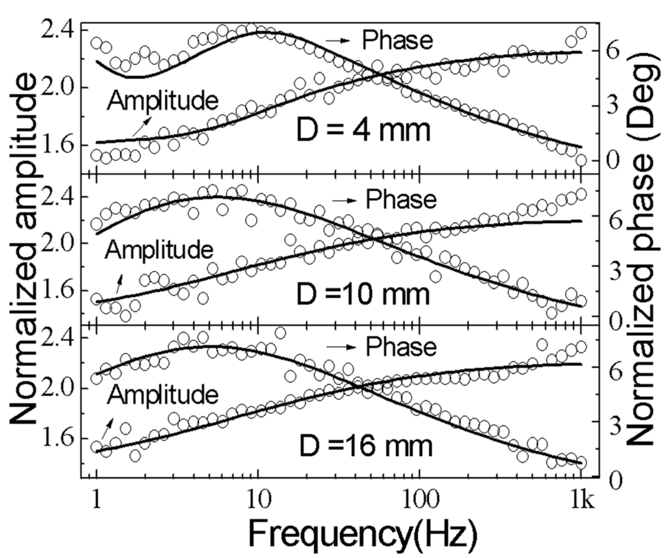

FIG. 9. PTR results. Symbols: experimental data; continuous lines: theoretical best fits.

TABLE I. Best-fit result of cylindrical rods based on cylindrical model Eq. (15).

Diameter (mm)	k1 (W/mK)	Lo (mm)	Q (mm^{-1})	φ (Degree)
4	15.06	1.05	3100	80.7
10	16.49	1.15	3610	82.6
16	16.46	1.07	3580	85.0

the higher carbon content on the outer surface becomes hardened via transformation from austenite to martensite, while the core remains soft in the form of ferritic and/or pearlite microstructure. After carburizing, the actual case depth was measured using the conventional mechanical indentation method. The other set was kept unhardened as a uniform reference. The cylindrical samples were fixed on a sample holder freely translating horizontally and vertically. The measuring point on the cylindrical sample was far away from the contact area between the sample and the holder, so thermal perturbations due to the contact were negligible. The thermal diffusivity of AISI 1020 steel was taken to be $\alpha_N = 13.7663 \times 10^{-6}\ m^2 s^{-1}$ (Ref. 20).

In the experiment, the illumination laser spot was expanded and collimated to about 20 mm in diameter so as to cover the whole surface of the cylindrical samples and also meet the requirement of uniform illumination along the axial direction assumed in the theory. It is estimated that, when $f = 1\,Hz$, the thermal diffusion length $\mu \approx 2\,mm$ [$\mu(f) = \sqrt{\alpha/\pi f}$]. Therefore, the 20 mm-illumination spot-size can be considered large enough when compared with the thermal diffusion length, the requirement of the uniform illumination along axial direction can thus be met. Samples of the same size were positioned carefully at the focal point of the paraboloidal mirror. The North Pole point of the cylindrical rods, with 90° azimuthal angle, was illuminated. The signal from the hardened sample was normalized with respect to an unhardened sample of the same material and diameter.

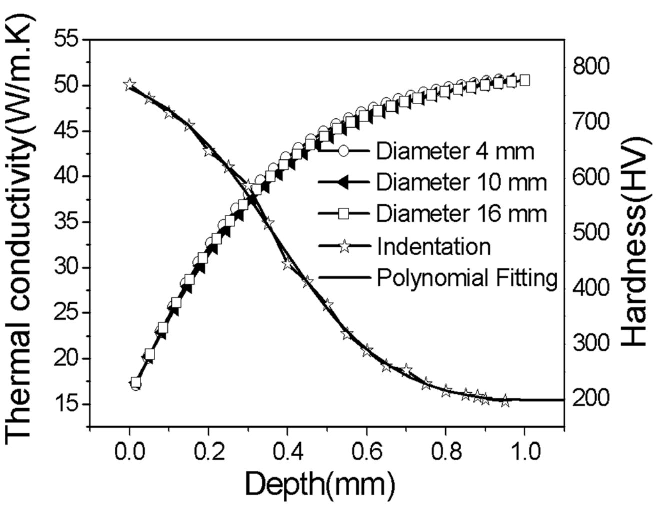

FIG. 10. Reconstructed depth profiles of the thermal conductivity of hardened cylindrical steel rods (left axis) and the microhardness profiles (right axis).

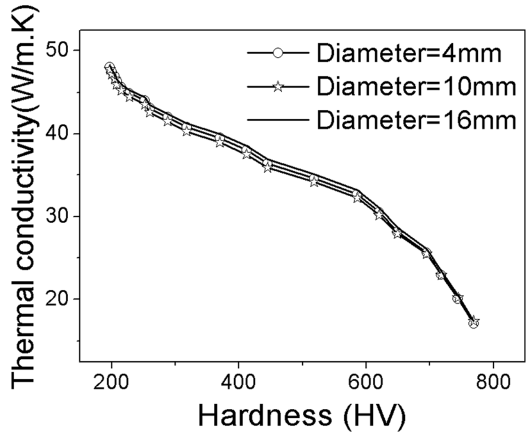

FIG. 11. The correlation between reconstructed thermal conductivity and the destructively measured hardness.

Figure 9 shows the normalized experimental results for samples with diameters of 4, 10 and 16 mm, respectively. These results are in agreement with our theoretical and computational simulations. We fitted the experimental data to the foregoing theoretical model developed by the Green-function method and the results are shown in Fig. 9, while the detailed best-fit parameters are shown in Table I. In the fitting process, diameter D and thermal conductivity of the unhardened core part k_0 are set as known parameters, whereas thermal conductivity of the surface k_N, depth of hardening L_0, and thermal gradient Q are set as fitting parameters. In addition, considering the fact that the absolute amplitude is meaningless and arbitrary because it is a function of many experimental factors, such as surface conditions (absorption coefficient), detector amplification factor etc., and an amplitude multiplication factor is used as a fitting parameter. In the inversion only the relative amplitude versus frequency is crucial to the fitting. It is seen that all best fitted results show excellent agreement with the data. The reconstructed thermal conductivity depth profile and the destructively measured hardness profile for these samples are shown in Fig. 10. It can be seen in the figure that the thermal conductivity profile exhibits good anticorrelation with the steel-hardness profile measured with the destructive indentation method. The detailed relationship between the reconstructed thermal conductivity and the destructively measured hardness can be extracted from Fig. 10, and is shown in Fig. 11. It is seen that the obtained anti-correlation is the same as those observed in Ref. 21, although the detailed hardness versus thermal conductivity values are different from those in the reference due to the different steel samples.

V. CONCLUSIONS

We have developed a theoretical thermal-wave model suitable for characterizing multi-layered cylindrical samples using optical heating from a laser beam with arbitrary intensity spatial profile. Based on the Green function method, the thermal-wave field from a multi-layered cylindrical sample with uniform surface illumination was obtained as a special case of a spatial heating profile. The thermal-wave dependencies on various thermophysical and geometrical parameters were also investigated. Together with our earlier investigations on composite cylindrical and spherical solids, this work complements the applications of thermal-wave techniques, and PTR in particular, in these two most commonly used curvilinear coordinate systems. With the advantages of the Green-function method over the quadrupole method with regard to the arbitrariness of the photothermal source spatial profile and its ability to handle both homogeneous boundary conditions (proper Green function) and inhomogeneous boundary conditions (improper Green function), this model offers a general analytical tool for characterizing cylindrical solids, photothermally excited with incident laser beams of varying spot sizes and angles of incidence, two parameters of direct experimental relevance.

ACKNOWLEDGMENTS

This work was supported by a grant from the National Natural Science Foundation of China (Grant No. 60877063), Scientific Research Foundation for Returned Scholars, Ministry of Education of China, and the project of the Priority Academic Program Development (PAPD)of Jiangsu Higher Education Institutions. The Canada Research Chairs and the Natural Sciences and Engineering Research Council of Canada are gratefully acknowledged for their support through a CRC Tier I award and a Discovery Grant, respectively, to A.M.

APPENDIX: THERMAL-WAVE GREEN FUNCTION FOR A MULTI-LAYERED CYLINDRICAL STRUCTURE

To calculate the Green function for a multi-layered cylinder with nonhomogeneous boundary conditions at the interface between the outer and inner layers, the following two related problems must be solved.

I. The Green function and spatial impulse-response functions for an infinitely long multi-layered cylinder with a spatially impulsive time-harmonic thermal-wave source at (r_0, φ_0), $r_{N-1} \le r_0 \le r_N$. A homogeneous Neumann boundary condition is prescribed at $r = r_N$.

In regions j, $[j = 1, 2, \ldots, (N-1)]$, with thermophysical properties (k_j, α_j), the spatial impulse-response function $H_j(\vec{r}\,|\vec{r}_0;\omega)$ (not a Green function in the layer which does not include the thermal-wave Dirac delta-function source),[17] satisfies the homogeneous equation:

$$\frac{1}{r}\frac{\partial}{\partial r}\left[r\frac{\partial}{\partial r}H_j(\vec{r}\,|\vec{r}_0;\omega)\right] + \frac{1}{r^2}\frac{\partial^2}{\partial\varphi^2}H_j(\vec{r}\,|\vec{r}_0;\omega) - \sigma_j^2(\omega)H_j(\vec{r}\,|\vec{r}_0;\omega) = 0. \quad \text{(A1)}$$

In region $N(r_{N-1} \le r \le r_N)$, with thermophysical properties (k_N, α_N), the Green function $G^{(N)}(\vec{r}|\vec{r}_0;\omega)$ satisfies:[17]

$$\frac{1}{r}\frac{\partial}{\partial r}\left[r\frac{\partial}{\partial r}G^{(N)}(\vec{r}|\vec{r}_0;\omega)\right] + \frac{1}{r^2}\frac{\partial^2}{\partial\varphi^2}G^{(N)}(\vec{r}|\vec{r}_0;\omega) - \sigma_N^2(\omega)G^{(N)}(\vec{r}|\vec{r}_0;\omega) = -\frac{\delta(r-r_0)\delta(\varphi-\varphi_0)}{\alpha_N r} \quad \text{(A2)}$$

$\sigma_j = (1+i)\sqrt{\omega/2\alpha_j}$, $(j = 1, 2, \ldots, N)$, and σ_j is the complex thermal wave number. The polar Dirac delta function can be expanded in the basis of the complete set of angular polar eigenfunctions:

$$\delta(\varphi - \varphi_0) = \frac{1}{2\pi}\sum_{m=-\infty}^{\infty} e^{im(\varphi-\varphi_0)}. \quad \text{(A3)}$$

Both the Green function in region N and the impulse-response function in regions j, $[j = 1, 2, \cdots, (N-1)]$ can be expanded in the same basis:

$$H_j(\vec{r}\,|r_0;\omega) = \frac{1}{2\pi}\sum_{m=-\infty}^{\infty} h_{jm}(r, r_0;\omega)\cdot e^{im(\varphi-\varphi_0)} \quad \text{(A4)}$$

$$G^{(N)}(\vec{r}|r_0;\omega) = \frac{1}{2\pi}\sum_{m=-\infty}^{\infty} g^{(N)}(r, r_0;\omega)\cdot e^{im(\varphi-\varphi_0)}. \quad \text{(A5)}$$

Substituting (A4) into (A1), we obtain:

$$h_jm(r, r_0;\omega) = a_jmI_m(\sigma_j r) + b_jmK_m(\sigma_j r), \quad (r_{j-1} \le r \le r_j, j = 1, r_{j-1} \equiv 0), \quad \text{(A6)}$$

where $j \in N^*, 1 \le j \le N-1$ and $b_{1m} \equiv 0$ when $j = 1$ [because $K_m(\sigma_1 r)$ becomes unbounded as $r \to 0$].

Substituting (A5) and (A3) into (A2), we obtain

$$\frac{1}{r}\frac{d}{dr}\left[r\frac{\partial}{\partial r}g_m^{(N)}(r, r_0;\omega)\right] - \left[\sigma_N^2 + \frac{m^2}{r^2}\right]g_m^{(N)}(r, r_0;\omega) = -\frac{\delta(r-r_0)}{\alpha_N r}, \quad (r_{N-1} \le r \le r_N). \quad \text{(A7)}$$

When $r \ne r_0$, Eq. (A7) reduces to a homogenous equation. Its solution can be shown to be

$$g_m^{(N)}(r, r_0;\omega) = \begin{cases} a_{Nm}I_m(\sigma_N r) + b_{Nm}K_m(\sigma_N r), (r_{N-1} \le r \le r_0) \\ a_{Nm}I_m(\sigma_N r) + b_{Nm}K_m(\sigma_N r) + \dfrac{I_m(\sigma_N r)K_m(\sigma_N r_0) - I_m(\sigma_N r_0)K_m(\sigma_N r)}{f(r_0)W(\sigma_N r_0)}, (r_0 \le r \le r_N) \end{cases} \quad \text{(A8)}$$

where we use the Green function reciprocity property and the Wroskian identity

$$W(\sigma_N r_0) \equiv I_m(\sigma_N r_0)K_m'(\sigma_N r_0) - I_m'(\sigma_N r_0)K_m(\sigma_N r_0) = -\frac{1}{r_0}$$

for the functions $I_m(\sigma_N r)$ and $K_m(\sigma_N r)$. $f(r_0) = \alpha_N r_0$. The coefficients of these $(2N-1)$ equation solutions can be related through the following boundary conditions of thermal-wave field and flux continuity:

In the exterior surface of region j, $r = r_j$; $(1 \le j \le N-2)$,

$$H_j(\vec{r}|\vec{r}_0;\omega)|_{r=r_j} = H_{j+1}(\vec{r}|\vec{r}_0;\omega)|_{r=r_j} \quad \text{(A9)}$$

$$k_j \frac{\partial H_j(\vec{r}|\vec{r}_0;\omega)}{\partial r}\bigg|_{r=r_j} = k_{j+1}\frac{\partial H_{j+1}(\vec{r}|\vec{r}_0;\omega)}{\partial r}\bigg|_{r=r_j}. \quad \text{(A10)}$$

At $r = r_N$, the homogeneous Neumann condition is assumed:

$$\frac{\partial G^{(N)}(\vec{r}|\vec{r}_0;\omega)}{\partial r}\bigg|_{r=r_N} = 0. \quad \text{(A11)}$$

Substituting these boundary conditions (A9)–(A11) into (A6), and (A8), we obtain (for writing convenience, the subscript m is omitted

At $r = r_1$

$$a_1 I_m(\sigma_1 r_1) = a_2 I_m(\sigma_2 r_1) + b_2 K_m(\sigma_2 r_1) \quad \text{(A12)}$$

$$a_1 I'_m(\sigma_1 r_1) = \beta_{21}[a_2 I'_m(\sigma_2 r_1) + b_2 K'_m(\sigma_2 r_1)]. \quad \text{(A13)}$$

At $r = r_2$

$$a_2 I_m(\sigma_2 r_2) + b_2 K_m(\sigma_2 r_2) = a_3 I_m(\sigma_3 r_2) + b_3 K_m(\sigma_3 r_2) \quad \text{(A14)}$$

$$a_2 I'_m(\sigma_2 r_2) + b_2 K'_m(\sigma_2 r_2) = \beta_{32}[a_3 I'_m(\sigma_3 r_2) + b_3 K'_m(\sigma_3 r_2)] \ldots\ldots \quad \text{(A15)}$$

At $r = r_j$

$$a_j I_m(\sigma_j r_j) + b_j K_m(\sigma_j r_j) = a_{j+1} I_m(\sigma_{j+1} r_j) + b_{j+1} K_m(\sigma_{j+1} r_j) \quad \text{(A16)}$$

$$a_j I'_m(\sigma_j r_j) + b_j K'_m(\sigma_j r_j) = \beta_{j+1,j}[a_{j+1} I'_m(\sigma_{j+1} r_j) + b_{j+1} K'_m(\sigma_{j+1} r_j)] \ldots\ldots \quad \text{(A17)}$$

where j satisfies $1 \le j \le N-1$, $\beta_{j+1,j} \equiv k_{j+1}/k_j$.

At $r = r_N$

$$a_N I'_m(\sigma_N r_N) + b_N K'_m(\sigma_N r_N) = \frac{1}{\alpha_N}[I'_m(\sigma_N r_N) K_m(\sigma_N r_0) - I_m(\sigma_N r_0) K'_m(\sigma_N r_N)]. \quad \text{(A18)}$$

To solve these 2(N-1) algebraic equations, we can express the solutions most conveniently by use of a matrix method

$$\begin{bmatrix} a_2 \\ b_2 \end{bmatrix} = T_1 \begin{bmatrix} a_1 \\ b_1 \end{bmatrix}, \quad \text{(A19)}$$

$$\begin{bmatrix} a_3 \\ b_3 \end{bmatrix} = T_2 \begin{bmatrix} a_2 \\ b_2 \end{bmatrix}, \quad \text{(A20)}$$

$$\begin{bmatrix} a_4 \\ b_4 \end{bmatrix} = T_3 \begin{bmatrix} a_3 \\ b_3 \end{bmatrix}, \ldots\ldots, \quad \text{(A21)}$$

$$\begin{bmatrix} a_N \\ b_N \end{bmatrix} = T_{N-1} \begin{bmatrix} a_{N-1} \\ b_{N-1} \end{bmatrix}, \quad \text{(A22)}$$

So

$$\begin{bmatrix} a_N \\ b_N \end{bmatrix} = T_{N-1} T_{N-2} \cdots T_2 T_1 \begin{bmatrix} a_1 \\ b_1 \end{bmatrix}, \quad \text{(A23)}$$

and $b_1 \equiv 0$, $T_j = B_j^{-1} A_j$ with:

$$A_j = \begin{bmatrix} I_m(\sigma_j r_j), K_m(\sigma_j r_j) \\ I'_m(\sigma_j r_j), K'_m(\sigma_j r_j) \end{bmatrix},$$

$$B_j = \begin{bmatrix} I_m(\sigma_{j+1} r_j), K_m(\sigma_{j+1} r_j) \\ \beta_{j+1,j} I'_m(\sigma_{j+1} r_j), \beta_{j+1,j} K'_m(\sigma_{j+1} r_j) \end{bmatrix}, \quad \text{(A24)}$$

We are only interested in a_N, b_N, which are parameters of the experimentally accessible surface thermal-wave field. Therefore, we can avoid solving for a_1 by defining:

$$T_{N-1} T_{N-2} \cdots T_2 T_1 \equiv \begin{bmatrix} t_{11}^{(N)}, t_{12}^{(N)} \\ t_{21}^{(N)}, t_{22}^{(N)} \end{bmatrix}. \quad \text{(A25)}$$

So $a_N = t_{11}^{(N)} a_1$ and $b_N = t_{21}^{(N)} a_1$

Also $(b_N/a_N) = (t_{21}^{(N)}/t_{11}^{(N)})$, which, combined with (A18) yield

$$a_N[I'_m(\sigma_N r_N) t_{11}^{(N)} + K'_m(\sigma_N r_N) t_{21}^{(N)}] = \frac{t_{11}^{(N)}}{\alpha_N}[I'_m(\sigma_N r_N) K_m(\sigma_N r_0) - I_m(\sigma_N r_0) K'_m(\sigma_N r_N)]. \quad \text{(A26)}$$

Finally, the solution is:

$$a_N = \frac{t_{11}^{(N)}}{\alpha_N[I'_m(\sigma_N r_N) t_{11}^{(N)} + K'_m(\sigma_N r_N) t_{21}^{(N)}]} \times [I'_m(\sigma_N r_N) K_m(\sigma_N r_0) - I_m(\sigma_N r_0) K'_m(\sigma_N r_N)], \quad \text{(A27)}$$

$$b_N = \frac{t_{21}^{(N)}}{\alpha_N[I'_m(\sigma_N r_N) t_{11}^{(N)} + K'_m(\sigma_N r_N) t_{21}^{(N)}]} \times [I'_m(\sigma_N r_N) K_m(\sigma_N r_0) - I_m(\sigma_N r_0) K'_m(\sigma_N r_N)]. \quad \text{(A28)}$$

Upon defining:

$$g_m^{(N)}(r, r_0;\omega) = \begin{cases} g_m^{<}(r, r_0;\omega), (r_{N-1} \le r \le r_0) \\ g_m^{>}(r, r_0;\omega), (r_0 \le r \le r_N) \end{cases} \quad \text{(A29)}$$

with

$$g_m^{<}(r, r_0;\omega) = \frac{[I_m(\sigma_N r) t_{11}^{(N)} + K_m(\sigma_N r) t_{21}^{(N)}]}{\alpha_N[I'_m(\sigma_N r_N) t_{11}^{(N)} + K'_m(\sigma_N r_N) t_{21}^{(N)}]} \times [I'_m(\sigma_N r_N) K_m(\sigma_N r_0) - I_m(\sigma_N r_0) K'_m(\sigma_N r_N)] \times (r_{N-1} \le r \le r_0) \quad \text{(A30)}$$

and

$$g_m^{>}(r, r_0;\omega) = \frac{[I_m(\sigma_N r_0) t_{11}^{(N)} + K_m(\sigma_N r_0) t_{21}^{(N)}]}{\alpha_N[I'_m(\sigma_N r_N) t_{11}^{(N)} + K'_m(\sigma_N r_N) t_{21}^{(N)}]} \times [I'_m(\sigma_N r_N) K_m(\sigma_N r) - I_m(\sigma_N r) K'_m(\sigma_N r_N)] \times (r_0 \le r \le r_N) \quad \text{(A31)}$$

where $t_{11}^{(N)}, t_{21}^{(N)}$ are obtained from Eq. (25), one finds:

$$G^{(N)}(\vec{r}|\vec{r}_0;\omega) = \begin{cases} G^{<}(\vec{r}|\vec{r}_0;\omega), & (r_{N-1} \le r \le r_0) \\ G^{>}(\vec{r}|\vec{r}_0;\omega), & (r_0 \le r \le r_N) \end{cases} \tag{A32}$$

$$G^{<}(\vec{r}|\vec{r}_0;\omega) = \frac{1}{2\pi\alpha_N}\sum_{m=-\infty}^{\infty} e^{im(\varphi-\varphi_0)} \times \frac{[I_m(\sigma_N r)t_{11}^{(N)} + K_m(\sigma_N r)t_{21}^{(N)}]}{[I'_m(\sigma_N r_N)t_{11}^{(N)} + K'_m(\sigma_N r_N)t_{21}^{(N)}]} \times [I'_m(\sigma_N r_N)K_m(\sigma_N r_0) - I_m(\sigma_N r_0)K'_m(\sigma_N r_N)], \times (r_{N-1} \le r \le r_0) \tag{A33}$$

$$G^{>}(\vec{r}|\vec{r}_0;\omega) = \frac{1}{2\pi\alpha_N}\sum_{m=-\infty}^{\infty} e^{im(\varphi-\varphi_0)} \times \frac{[I_m(\sigma_N r_0)t_{11}^{(N)} + K_m(\sigma_N r_0)t_{21}^{(N)}]}{[I'_m(\sigma_N r_n)t_{11}^{(N)} + K'_m(\sigma_N r_N)t_{21}^{(N)}]} \times [I'_m(\sigma_N r_N)K_m(\sigma_N r) - I_m(\sigma_N r)K'_m(\sigma_N r_N)], \times (r_0 \le r \le r_N). \tag{A34}$$

A. Special case: Two-layer cylinder

When $N = 2$,

$$B_1^{-1}A_1 = \frac{(-r_1)}{\beta_{21}}\begin{bmatrix} \beta_{21}K'_m(\sigma_2 r_1), -K_m(\sigma_2 r_1) \\ -\beta_{21}I'_m(\sigma_2 r_1), I_m(\sigma_2 r_1) \end{bmatrix}\begin{bmatrix} I_m(\sigma_1 r_1), K_m(\sigma_1 r_1) \\ I'_m(\sigma_1 r_1), K'_m(\sigma_1 r_1) \end{bmatrix}$$
$$= c\begin{bmatrix} \beta_{21}K'_m(\sigma_2 r_1)I_m(\sigma_1 r_1) - K_m(\sigma_2 r_1)I'_m(\sigma_1 r_1), & \beta_{21}K'_m(\sigma_2 r_1)K_m(\sigma_1 r_1) - K_m(\sigma_2 r_1)K'_m(\sigma_1 r_1) \\ -[\beta_{21}I'_m(\sigma_2 r_1)I_m(\sigma_1 r_1) - I_m(\sigma_2 r_1)I'_m(\sigma_1 r_1)], & -[\beta_{21}I'_m(\sigma_2 r_1)K_m(\sigma_1 r_1) - I_m(\sigma_2 r_1)K'_m(\sigma_1 r_1)] \end{bmatrix}$$

where

$$c \equiv -r_1/\beta_{21}. \tag{A35}$$

Therefore,

$$t_{11}^{(2)} = c[\beta_{21}K'_m(\sigma_2 r_1)I_m(\sigma_1 r_1) - K_m(\sigma_2 r_1)I'_m(\sigma_1 r_1)], \tag{A36}$$

$$t_{21}^{(2)} = -c[\beta_{21}I'_m(\sigma_2 r_1)I_m(\sigma_1 r_1) - I_m(\sigma_2 r_1)I'_m(\sigma_1 r_1)], \tag{A37}$$

By substituting (A36), (A37) into (A32), we obtain the known Green function of a bilayered cylindrical structure,[5] as expected, upon symbol substitution: $a \to r_1, b \to r_2$.

II. Equivalence relation between a multi–layer composite cylinder with homogeneous Neumann conditions at the exterior surface of region N ($r = r_N$)(Section A.I) and a hollow cylinder[6] with one homogeneous Neumann condition at $r = b \to r_N$ (exterior surface), namely $m_2 = 0$, and another homogeneous third-kind boundary condition at the interior surface $r = a \to r_{N-1}$

From Sec. A.I, the Green function Eq. (A32), evaluated at $r = r_{N-1}$ is found to be

$$G^{(N)}(\vec{r}_{N-1}|\vec{r}_0;\omega) = \frac{1}{2\pi\alpha_n}\sum_{m=-\infty}^{\infty} e^{im(\varphi-\varphi_0)} \times \frac{[I_m(\sigma_N r_{N-1})t_{11}^{(N)} + K_m(\sigma_N r_{N-1})t_{21}^{(N)}]}{[I'_m(\sigma_N r_N)t_{11}^{(N)} + K'_m(\sigma_N r_N)t_{21}^{(N)}]} \times [I'_m(\sigma_N r_N)K_m(\sigma_N r_0) - I_m(\sigma_N r_0)K'_m(\sigma_N r_N)] \tag{A38}$$

and

$$\begin{bmatrix} t_{11}^{(N)} \\ t_{21}^{(N)} \end{bmatrix} = T_{N-1}\begin{bmatrix} t_{11}^{(N-1)} \\ t_{21}^{(N-1)} \end{bmatrix} \tag{A39}$$

$$T_{N-1} = B_{N-1}^{-1}A_{N-1} = \frac{-r_{N-1}}{\beta_{N,N-1}}\begin{bmatrix} \beta_{N,N-1}K'_m(\sigma_N r_{N-1}), -K_m(\sigma_N r_{N-1}) \\ -\beta_{N,N-1}I'_m(\sigma_N r_{N-1}), I_m(\sigma_N r_{N-1}) \end{bmatrix} \times \begin{bmatrix} I_m(\sigma_{N-1}r_{N-1}), K_m(\sigma_{N-1}r_{N-1}) \\ I'_m(\sigma_{N-1}r_{N-1}), K'_m(\sigma_{N-1}r_{N-1}) \end{bmatrix}.$$

If we define $c = \frac{-r_{N-1}}{\beta_{N,N-1}}$, then

$$I_m(\sigma_N r_{N-1})t_{11}^{(N)} + K_m(\sigma_N r_{N-1})t_{21}^{(N)} = \frac{c}{-r_{N-1}}\beta_{N,N-1}[I_m(\sigma_{N-1}r_{N-1})t_{11}^{(N-1)} + K_m(\sigma_{N-1}r_{N-1})t_{21}^{(N-1)}] \tag{A40}$$

and

$$I'_m(\sigma_N r_N)t_{11}^{(N)} + K'_m(\sigma_N r_N)t_{21}^{(N)} = c\{\beta_{N,N-1}[I_m(\sigma_{N-1}r_{N-1})t_{11}^{(N-1)} + K_m(\sigma_{N-1}r_{N-1})t_{21}^{(N-1)}][I'_m(\sigma_N r_N)K'_m(\sigma_N r_{N-1}) - I'_m(\sigma_N r_{N-1})K'_m(\sigma_N r_N)] + [I'_m(\sigma_{N-1}r_{N-1})t_{11}^{(N-1)} + K'_m(\sigma_{N-1}r_{N-1})t_{21}^{(N-1)}][I_m(\sigma_N r_{N-1})K'_m(\sigma_N r_N) - I'_m(\sigma_N r_N)K_m(\sigma_N r_{N-1})]\}. \tag{A41}$$

Now the Green function can be re-arranged as follows:

$$G^{(N)}(\vec{r}_{N-1}|\vec{r}_0;\omega) = \frac{1}{2\pi\alpha_N}\sum_{m=-\infty}^{\infty} e^{im(\varphi-\varphi_0)} \times \frac{[K_m(\sigma_N r_0)I'_m(\sigma_N r_N) - I_m(\sigma_N r_0)K'_m(\sigma_N r_N)]/(-r_{N-1})}{[I'_m(\sigma_N r_N)K'_m(\sigma_N r_{N-1}) - I'_m(\sigma_N r_{N-1})K'_m(\sigma_N r_N)] + \lambda_{N-1}[I_m(\sigma_N r_{N-1})K'_m(\sigma_N r_N) - I'_m(\sigma_N r_N)K_m(\sigma_N r_{N-1})]} \tag{A42}$$

where $\lambda_{N-1} \equiv \frac{[I'_m(\sigma_{N-1}r_{N-1})t_{11}^{(N-1)}+K'_m(\sigma_{N-1}r_{N-1})t_{21}^{(N-1)}]}{\beta_{N,(N-1)}[I_m(\sigma_{N-1}r_{N-1})t_{11}^{(N-1)}+K_m(\sigma_{N-1}r_{N-1})t_{21}^{(N-1)}]}$.

For a hollow cylinder, the Green function in the region N can be expressed as:[6]

$$G(\vec{r}|\vec{r}_0;\omega) = \frac{1}{2\pi\alpha}\sum_{m=-\infty}^{\infty}\frac{e^{im(\varphi-\varphi_0)}}{[Y_m(b)-X_m(a)]}\times\begin{cases}[K_m(\sigma r_0)-Y_m(b)I_m(\sigma r_0)][K_m(\sigma r)-X_m(a)I_m(\sigma r)],(a\le r\le r_0)\\ [K_m(\sigma r_0)-X_m(a)I_m(\sigma r_0)][K_m(\sigma r)-Y_m(b)I_m(\sigma r)],(r_0\le r\le b).\end{cases} \tag{A43}$$

where

$$X_m(a) \equiv \frac{[K'_m(\sigma a)-m_1K_m(\sigma a)]}{[I'_m(\sigma a)-m_1I_m(\sigma a)]} \tag{A44}$$

$$Y_m(b) \equiv \frac{[K'_m(\sigma b)+m_2K_m(\sigma b)]}{[I'_m(\sigma b)+m_2I_m(\sigma b)]} \tag{A45}$$

with

$$m_1 \equiv \frac{h_1}{k}, m_2 \equiv \frac{h_2}{k}. \tag{A46}$$

The Green function at $r = a$ can also be rearranged assuming $m_2 = 0$ corresponding to a homogeneous Neumann condition at $r = b$ (exterior surface), in order to compare it with the case described in Sec. AI.

Letting $\alpha = \alpha_N, k = k_N$, so that $\kappa = \kappa_N$ and $a \to r_{N-1}$, $b \to r_N$, $m_1 \to m_{(N-1)}$, assuming $r = r_{N-1}$, Eq. (A43) can be rearranged:

$$G(\vec{r}_{N-1}|\vec{r}_0;\omega) = \frac{1}{2\pi\alpha_N}\sum_{m=-\infty}^{\infty}e^{im(\varphi-\varphi_0)} \times\frac{[K_m(\sigma_N r_0)I'_m(\sigma_N r_N)-I_m(\sigma_N r_0)K'_m(\sigma_N r_N)]/r_{N-1}}{[I'_m(\sigma_N r_{N-1})K'_m(\sigma_N r_N)-I'_m(\sigma_N r_N)K'_m(\sigma_N r_{N-1})]+m_{(N-1)}[I'_m(\sigma_N r_N)K_m(\sigma_N r_{N-1})-I_m(\sigma_N r_{N-1})K'_m(\sigma_N r_N)]}. \tag{A47}$$

Comparison with (A42) and (A47), yields

$$m_{(N-1)} = \lambda_{N-1} \equiv \frac{[I'_m(\sigma_{N-1}r_{N-1})t_{11}^{(N-1)}+K'_m(\sigma_{N-1}r_{N-1})t_{21}^{(N-1)}]}{\beta_{N,(N-1)}[I_m(\sigma_{N-1}r_{N-1})t_{11}^{(N-1)}+K_m(\sigma_{N-1}r_{N-1})t_{21}^{(N-1)}]}. \times (N\ge 2), \tag{A48}$$

Upon defining $\gamma_{N,(N-1)\cdots 321} \equiv \gamma_{N!} \equiv \left[t_{21}^{(N)}/t_{11}^{(N)}\right]$, Eq. (A48) becomes

$$m_{(N-1)} = \frac{[I'_m(\sigma_{N-1}r_{N-1})+K'_m(\sigma_{N-1}r_{N-1})\cdot\gamma_{(N-1)\cdots 321}]}{\beta_{N,(N-1)}[I_m(\sigma_{N-1}r_{N-1})+K_m(\sigma_{N-1}r_{N-1})\cdot\gamma_{(N-1)\cdots 321}]}, \tag{A49}$$

with $m_{(N-1)} \equiv \left[h_{(N-1)}/k_N\right]$. Finally,

$$h_{(N-1)} = k_{(N-1)}\cdot\frac{[I'_m(\sigma_{N-1}r_{N-1})+K'_m(\sigma_{N-1}r_{N-1})\cdot\gamma_{(N-1)\cdots 321}]}{[I_m(\sigma_{N-1}r_{N-1})+K_m(\sigma_{N-1}r_{N-1})\cdot\gamma_{(N-1)\cdots 321}]} \tag{A50}$$

If $N = 2$, Eq. (A50) reduces to [Ref. 6, Eq. A34]

$$h_1 = k_1\cdot\frac{I'_m(\sigma_1 r_1)+K_m(\sigma_1 r_1)\gamma_1}{I_m(\sigma_1 r_1)+K_m(\sigma_1 r_1)\gamma_1} = k_1\frac{I'_m(\sigma_1 r_1)}{I_m(\sigma_1 r_1)}, (\gamma_1 \equiv 0).$$

As expected, on replacing the otherwise arbitrary constants $m_{(N-1)}$ and $h_{(N-1)}$ in Eq. (A43) with the foregoing expressions which contain thermal-wave parameters from the underlayer region N-I, the Green function (A32) can be transformed into a proper Green function for region N. As such, Equations (A43) with (A49) and (A50) satisfy the field Eq. (5) with those particular values of $m_{(N-1)}$ and $h_{(N-1)}$. Substituting $m_{(N-1)}$ and $h_{(N-1)}$ into Eq. (A46), one can obtain the Green function in region N, and taking $F_N(\vec{r}_N,\omega)$ in Eq. (5), after some algebraic manipulation one finally obtains the thermal-wave field, Eq. (15), in region N.

[1] *Non-Destructive Evaluation, Vol. 2 of the series: Progress in Photothermal and Photoacoustic Science and Technology*, edited by A. Mandelis (PTR-Prentice Hall, Englewood Cliffs, 1994).
[2] H. K. Park, C. P. Grigoropoulos, and A. C. Tam, Int. J. Thermophys. **16**, 973 (1995).

[3] R. Santos and L. C. M. Miranda, J. Appl. Phys. **52**, 4194 (1981).
[4] D. P. Almond and P. M. Patel, *Photothermal Science and Techniques* (Chapman and Hall, London, 1996).
[5] C. Wang, A. Mandelis, and Y. Liu, J. Appl. Phys. **96**, 3756 (2004).
[6] C. Wang, A. Mandelis, and Y. Liu, J. Appl. Phys. **97**, 014911 (2005).
[7] C. Wang, Y. Liu, A. Mandelis, and J. Shen, J. Appl. Phys. **101**, 083503 (2007).
[8] G. Xie, Z. Chen, C. Wang, and A. Mandelis, Rev. Sci. Instrum. **80**, 034903 (2009).
[9] A. Salazar,F. Garrido, and R. Celorrio, J. Appl. Phys. **99**, 066116 (2006).
[10] A. Salazar and R. Celorrio, J. Appl. Phys. **100**, 113535 (2006).
[11] N. Madariaga and A. Salazar, J. Appl. Phys. **101**, 103534 (2007).
[12] T. T. N. Lan, U. Seidel, and H. G. Walther, J. Appl. Phys. **77**, 4739 (1995).
[13] T. T. N Lan, U. Seidel, H. G. Walther, G. Goch, and B. Schmitz, J. Appl. Phys. **78**, 4108 (1995).
[14] M. Munidasa, F. Funak, and A. Mandelis, J. Appl. Phys. **83**, 3495 (1998).
[15] C. Glorieux, R. Li Voti, J. Thoen, M. Bertolotti, and C. Sibilia, J. Appl. Phys. **85**, 7059 (1999).
[16] H. Qu, C. Wang, X. Guo, and A. Mandelis, J. Appl. Phys. **104**, 113518 (2008).
[17] A. Mandelis, *Diffusion-Wave Fields: Mathematical Methods and Green Function* (Springer, New York, 2001), Chap. 6, pp. 90 and 413.
[18] A. Mandelis, F. Funak, and M. Munidasa, J. Appl. Phys. **80**, 5570 (1996).
[19] R. E. Imhof, B. Zhang, and D. J. S. Birch, *Progress in Photothermal and Photoacoustic Science and Technology, Vol. 2: Non-Destructive Evaluation* (PTR Prentice-Hall, Englewood Cliffs, 1994), Chap. 7.
[20] *Properties of selection: Iron, Steel of High Performance Alloys in Metals Handbook*, (ASM International, Material Park, 1990), Vol. 1, p. 196.
[21] H. G. Walther, D. Fournier, J. C. Krapez, M. Luukkala, B. Schmitz, C. Sibilia, H. Stamm, and J. Thoen, Anal Sci. **17**, s165 (2001).